This is the accepted manuscript made available via CHORUS. The article has been published as:

Ultrafast Photoinduced Phase Change in SnSe

Benjamin J. Dringoli, Mark Sutton, Zhongzhen Luo, Mercouri G. Kanatzidis, and David G. Cooke

Phys. Rev. Lett. **132**, 146901 — Published 1 April 2024

DOI: 10.1103/PhysRevLett.132.146901

Ultrafast Photo-induced Phase Change in SnSe

Benjamin J. Dringoli,[1] Mark Sutton,[1] Zhongzhen Luo,[2,3] Mercouri G. Kanatzidis,[2] and David G. Cooke[1,*]

[1] *Department of Physics, McGill University, Montreal, QC, Canada H3A2T8*
[2] *Department of Chemistry, Northwestern University, Evanston, Illinois 60208, United States*
[3] *Key Laboratory of Eco-Materials Advanced Technology, College of Materials Science and Engineering, Fuzhou University, Fuzhou 350108, P. R. China*

Time-resolved multi-terahertz (THz) spectroscopy is used to observe an ultrafast, non-thermal electronic phase change in SnSe driven by interband photoexcitation with 1.55 eV pump photons. The transient THz photoconductivity spectrum is found to be Lorentzian-like, indicating charge localization and phase segregation. The rise of photoconductivity is bimodal in nature, with both a fast and slow component due to excitation into multiple bands and subsequent intervalley scattering. The THz conductivity magnitude, dynamics, and spectra show a drastic change in character at a critical excitation fluence of approximately 6 mJ/cm^2 due to a photo-induced phase segregation and a macroscopic collapse of the band gap.

Tin Selenide (SnSe) is a quasi-two dimensional semiconductor exhibiting record-setting thermoelectric properties, with a figure-of-merit $ZT = 2.62$ along the in-plane b-axis [1–5]. A polar analogue of black phosphorous, at room temperature SnSe has a layered, orthorhombic $Pnma$ phase with zig-zag and armchair ordering shown in Fig. 1(a) and (b), respectively. In the $Pnma$ phase, it possesses an indirect band gap of 0.9 eV [6] and a direct gap of 1.21 eV [7], shown in Fig. 1(c). At $T_c = 807$ K, a $Pnma \rightarrow Cmcm$ structural phase transition occurs, reducing thermal conductivity due to phonon-phonon scattering arising from strong anharmonicity. The origin of this transition has been intensely studied in the past several years, being attributed to either a displacive transition typically seen in ferroelectrics or a dynamic order-disorder transition [8–16]. The displacive transition is primarily driven by atomic motion along the c-axis [17], accompanied by phonon softening and an eventual collapse of terahertz (THz) frequency zone center optical phonons [17–19]. Very recent neutron scattering measurements, however, support a disordered high temperature phase with local contributions from the $Pnma$ phase on length scales of a few unit cells [16]. Phonon anharmonicities in SnSe are driven by electronic bonding instabilities involving Se 4p-orbitals and Sn 5s-orbitals containing lone pair electrons [13, 19–24], whose states comprise the photoacessible Γ-valley valence band. Optical excitation can selectively perturb these deeper lying bands and reveal novel, thermally inaccessible phases.

Ultrafast scattering and spectroscopy can disentangle the complexity underlying these dynamic lattice instabilities [25–28], leading to a better understanding of the microscopic interactions underlying thermoelectric properties. Recently, structural probes such as ultrafast electron diffraction (UED)[29, 30], time-resolved x-ray diffraction (TR-XRD) [31, 32], and transient reflectivity (TR) measurements [33] have revealed novel, non-thermal structural dynamics following femtosecond excitation at photon energies of 1.55 eV ($\lambda_p = 800$ nm). These have indicated sub-picosecond transitions towards the $Cmcm$ phase driven by displacive excitation of A_g phonons [33], domain formation mediated by photoinduced interlayer strain fields [29], bimodal polaron formation [30], and transient atomic motions towards a thermally inaccessible $Immm$ phase [31, 32]. Given the diversity of structural phenomena indicated by these prior works, a complementary survey of the electronic behavior under these excitation conditions is needed.

In this work, we use ultra-broadband time-resolved terahertz (THz) spectroscopy to probe the electronic response of SnSe under identical excitation conditions as these previous ultrafast structural probe measurements ($\lambda_p = 800$ nm, $F = 0.1 - 13.2$ mJ/cm^2). We observe non-Drude THz conductivity spectra exhibiting bimodal formation dynamics consistent with previous UED work reporting polaron formation after ultrafast excitation [30]. Moreover, we find evidence for an electronic phase transition occurring at a critical pump excitation fluence $F_c \approx 6$ mJ/cm^2, where THz conductivity magnitude, dynamics and spectra change sharply. This excitation density is consistent with the proposed $Pnma \rightarrow Immm$ destabilization threshold [31].

Time-resolved THz spectroscopy (TRTS) was performed using single-cycle, multi-THz pulses shown in Supplemental Fig. 1(a). These pulses were generated by a two-color laser plasma in dry air, formed by co-focusing 35 fs-duration fundamental (800 nm) and second harmonic (400 nm) pulses from a 1 kHz amplified

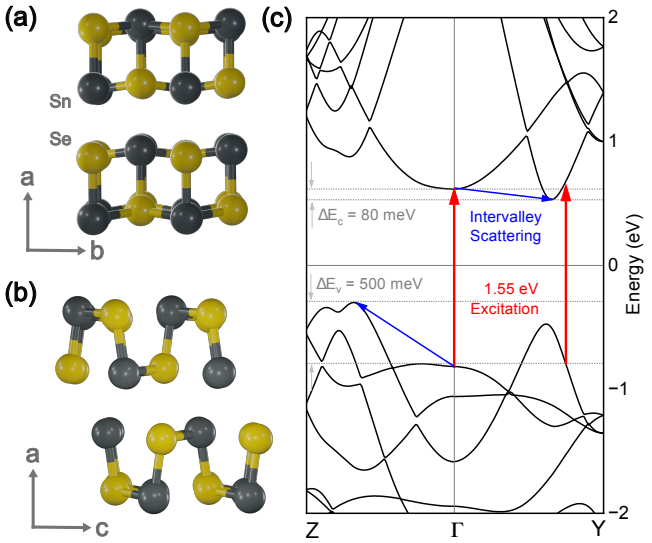

Figure 1. (a,b) SnSe layered atomic structure along the in-plane zigzag b-axis and armchair c-axis in the room temperature *Pnma* phase (c) *Pnma*-phase SnSe electronic band structure from *ab initio* calculations using data provided from Ref. [5] with permission from the authors. Red arrows show carrier excitation from the 1.55 eV pump, blue arrows show post-excitation relaxation pathways to band extrema.

Ti:Sapphire femtosecond laser system [34–38]. These multi-THz pulses contain Fourier components continuously covering a $1-20$ THz spectral range ($4-85$ meV), as shown in Supplemental Fig. 1(b). A schematic of the spectrometer is shown in Supplemental Fig. 2 and further details on the setup are provided in Ref. [25]. The SnSe sample was a 3 mm x 5 mm x 3.6 mm, high quality single crystal of SnSe grown using methods as described in Ref. [1], and from the same parent crystal as in Ref. [30]. The crystal was measured via reflection at normal incidence with the THz and pump pulses linearly polarized along the b-axis. Other crystal orientations were measured, with results shown in Supplemental Fig. 3, however no significant change in response was observed.

The reflected THz field was directly sampled in time t using air-biased coherent detection at various pump-probe delay times τ [34, 39]. Both the reflected field in the presence of a pump pulse, $E_p(t,\tau)$, and the differential $\Delta E(t,\tau) = E_p(t,\tau) - E_r(t)$ are measured simultaneously in a double-modulation scheme [40], where $E_r(t)$ is the reference THz field reflected from the unexcited sample. The pulse delays are implemented such that all points in the measured THz fields have experienced a constant τ, so a Fourier transformation along the real time axis t is devoid of any convolution artifacts and directly provides a temporal snapshot of the frequency-dependent response [41]. Intrinsic artifacts that can appear in TRTS, as mentioned in Ref. [42], are not present (see Supplemental Fig. 4) as carrier momentum relaxation times are extremely short [43]. The pump-induced differential reflectivity $\Delta\tilde{r}(\omega,\tau)/r_0(\omega) = \Delta E(\omega,\tau)/E_r(\omega) - 1$, where $r_0(\omega)$ is the static reflectivity, was subsequently extracted by Fourier analysis. The static $r_0(\omega)$ is dominated by a single reststrahlen band for THz polarization parallel to the b-axis [44], shown in Supplemental Fig. 1, which prohibits the extraction of the optical conductivity below ~5 THz. The THz reflectivity is finally related to the pump-induced differential optical conductivity $\Delta\tilde{\sigma}(\omega,\tau) = \Delta\sigma_1(\omega,\tau) + i\Delta\sigma_2(\omega,\tau)$ by modelling the photoexcited layer as a slab by [45]:

$$\Delta\tilde{\sigma}(\omega,\tau) = \frac{1}{Z_0 d}\frac{(\Delta\tilde{r}/r_0)(\tilde{n}^2-1)}{(\Delta\tilde{r}/r_0)(1-\tilde{n})+2}, \qquad (1)$$

where $d = 60$ nm is the pump penetration depth at $\lambda = 800$ nm [46], $Z_0 = 377\ \Omega$ is the impedance of free space, and $\tilde{n}(\omega)$ is the static complex THz refractive index [44]. Despite reports of saturable absorption in SnSe nanosheets at much lower peak powers [47], the pump absorption was found to be independent of excitation fluence and average heating of the sample surface was estimated by infrared imaging to be $< 15°$C, shown in Supplemental Figs. 5 and 6, respectively.

Two-dimensional $\Delta\sigma_1(\omega,\tau)$ maps for frequencies above all phonon branches ($\omega/2\pi > 5.5$ THz), where the electronic intraband response dominates, are shown in Fig. 2 for pump fluences of (a) 1.8 mJ/cm^2 and (b) 12.0 mJ/cm^2. Additional 2D maps for varying fluences are presented in Supplemental Fig. 7. In both low and high fluence regimes, the conductivity has Lorentzian character despite all assumptions of SnSe being a band semiconductor where the expectation is a simple Drude response. Such a broadened Lorentzian response can arise from phase heterogeneity and the formation of domains that favor conduction over smaller length scales (higher frequencies), which has been observed in SnSe at these fluences [29]. The optical conductivity of a heterogeneous phase system is usually described by effective medium theories (e.g. Bruggeman), and typically displays a monotonically increasing $\sigma_1(\omega)$ from zero frequency [48]. However, here $\sigma_1(\omega)$ exhibits a clear onset at the LO phonon energy

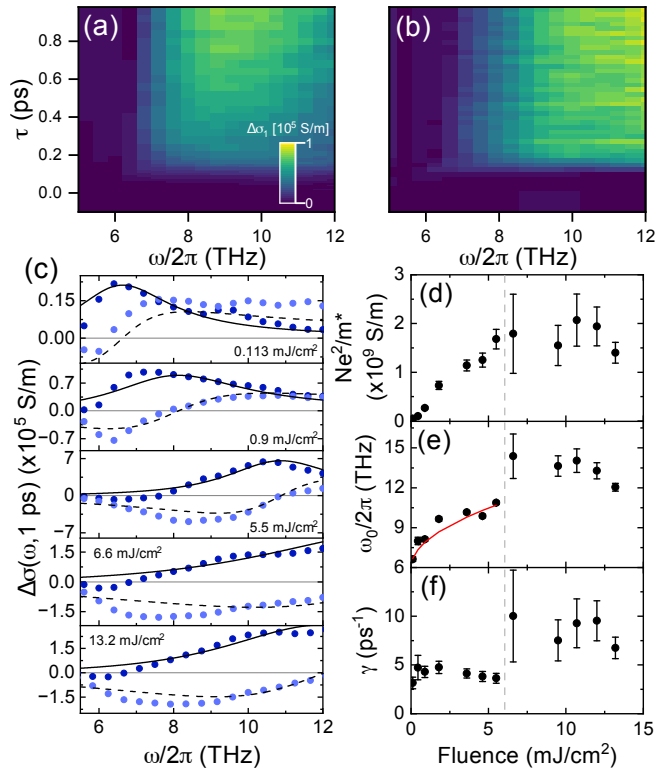

Figure 2. (a,b) Two-dimensional real conductivity $\Delta\sigma_1(\omega,\tau)$ maps for 1.8 and 12.0 mJ/cm^2. (c) Complex THz differential photoconductivity spectra $\Delta\tilde{\sigma}(\omega,\tau)=\sigma_1(\omega,\tau)+i\sigma_2(\omega,\tau)$ for various fluences. $\Delta\sigma_1(\omega,\tau=1$ ps) shown in dark colors, $\Delta\sigma_2(\omega,\tau=1$ ps) shown in light colors, and Lorentzian fits shown in black solid and dashed lines. Note the significant difference in vertical axis scales. Fluence dependence of the (d) Lorentzian oscillator strength Ne^2/m^*, (e) center frequency ω_0, and (f) linewidth γ. ω_0 is fitted with a scaled $\sqrt{F}$ function, shown in red and discussed in the text.

of $\sim$ 20 meV ($\sim$ 5 THz). This could indicate that photoexcited carriers are polarons [49], as suggested by calculations showing strong electron-phonon coupling near Γ [50] and previous UED measurements indicating the formation of a 3D polaron with radius $\sim$ 4.2 Å after photoexcitation [30].

To quantify the evolution of spectral shape, we fit the data to a Lorentzian response given by

$$\Delta\tilde{\sigma}(\omega)=\frac{Ne^2}{m^*}\frac{\omega}{i(\omega_0^2-\omega^2)+\omega\gamma} \qquad (2)$$

with Ne^2/m^* as the oscillator strength, ω_0 the resonance frequency, and γ the scattering rate. This simple phenomenological model fits both σ_1 and σ_2 reasonably well over the entire fluence regime for all times, as shown in Fig. 2(c) and in Supplemental Fig. 8. The fit parameters Ne^2/m^*, ω_0, and γ for all fluences are shown in Fig. 2(d),(e) and (f), respectively. Two fluence regimes are identified: a low ($F<6.6$ mJ/cm^2) and a high ($F\geq 6.6$ mJ/cm^2) fluence regime. In the low fluence regime, Ne^2/m^* increases linearly and monotonically with fluence, as expected for unsaturated interband excitation of charge carriers. The scattering rate γ remains relatively constant in this fluence range, reflecting consistency of the absorption pathways shown in Fig. 1(c) for these fluences. The fitted ω_0 scales with an approximately $\sqrt{F}$ dependence just above LO phonon energy. Localization of charges is implied in a Lorentzian response, however the increase of ω_0 with fluence is inconsistent with models of weak localization [51] or backscattering [52]. Instead, this implies a plasmonic origin where such a $\omega_0\propto\sqrt{F}$ dependence is expected for a heterogeneous medium, provided there is isolation of neighboring conducting domains such that depolarization fields contribute [48, 53]. The long-time relaxation of the system, shown in Supplemental Fig. 9, occurs on a $\sim$150 ps time scale, consistent with previous measurements reporting interband recombination [54]. This relaxation is also seen in the redshifting of the spectral peak at long times shown in Supplemental Fig. 10, again consistent with a system of heterogeneous conductive media. At a critical fluence $F_c=6.6$ mJ/cm^2, a discontinuous increase in ω_0 and γ occurs while Ne^2/m^* saturates. This sudden change suggests a charge density-driven electronic phase transition occurring on ultrafast time scales.

Further evidence for an electronic phase transition is seen in the dynamics of $\sigma_1(\omega,\tau)$, monitored at $\omega/2\pi=$ 10 THz, far above all phonon branches and where $\Delta\sigma$ is dominated by electronic excitations. Fig. 3(a-e) shows the clear bimodal dynamics in the sub-picosecond manifestation of photoconductivity. In the low fluence regime, there are two distinct components: a 40 fs instrument response-limited rise after photoexcitation and a slower $\sim$200 fs rise. Examining the *Pnma* band structure shown in Fig. 1(c), we can classify pump absorption into two main channels: 1) excitation into the high effective mass, non-dispersive bands about the Γ-point which subsequently undergo interband scattering to the lower-mass band extrema; and 2) excitation of hot, mobile charge carriers distributed throughout the Brillouin zone that cool via intraband relaxation. The Γ valley carriers have an effective mass of $1.20m_e$ [2], eight times that of band extrema along $\Gamma-Y$ and $\Gamma-Z$ at $0.15m_e$ [55]. Therefore, the measured THz conductivity is dominated by n_{free}, with

the slow rise representing the scattering of heavier n_Γ carriers to the extrema, enabled through the high electron-phonon coupling near the Γ point [50]. The conductivity dynamics can therefore be well fit by a two-component rate equation model:

$$\begin{aligned}\frac{dn_\Gamma(t)}{dt} &= \eta\ \exp[-(t/\sqrt{2}\tau_p)^2)] - n_\Gamma(t)\gamma_{inter} \\ \frac{dn_{\text{free}}(t)}{dt} &= (1-\eta)\exp[-(t/\sqrt{2}\tau_p)^2)] + n_\Gamma(t)\gamma_{inter} \\ \Delta\sigma_1(t) &= A\left(\frac{e\tau}{m_f^*}n_{\text{free}}(t) + \frac{e\tau}{m_\Gamma^*}n_\Gamma(t)\right).\end{aligned} \quad (3)$$

Here n_Γ, n_{free} are the populations in the Γ and mobile bands, respectively, η is the fraction of charge carriers excited into the Γ valley, τ_p is the pump pulse duration, e is the electron charge, A is an amplitude scaling factor, and m^* are the effective masses. As a simplifying assumption, the momentum scattering time τ is assumed to be 20 fs for both populations[43]. The intervalley scattering rate, $\gamma_{inter} \approx 1-2$ THz, is typical of polar semiconductors at room temperature [56]. When $F \geq 6.6$ mJ/cm^2, the same fluence where the spectra sharply blue shifted, the magnitude of the response A drops sharply as shown in Fig. 3(f). At the same fluence, the slow scattering process and associated rise in conductivity, represented by η and shown in Fig. 3(g), vanishes and only recovers slightly at the higher fluence. This indicates the sudden elimination of intervalley scattering from the Γ-valley. Such a drastic change in the magnitude, spectra and dynamics of intraband conductivity at F_c is a strong indication of a photo-induced, ultrafast change of macroscopic phase over THz wavelength length scales.

A photo-induced *Pnma-Immm* structural phase transition was recently observed in SnSe accompanied by a fluence-dependent softening of A_g phonon modes [31]. This Peierls-like structural instability is driven by the removal of electrons in nondispersive electronic bands derived from both Se 4*px*- and Sn 5*s*-orbitals [32], which form the non-dispersive bands at Γ [13]. The authors estimated the *Pnma* phase is fully destabilized in favor of the *Immm* phase at a photoexcited carrier density of 0.2 holes per formula unit, corresponding to 9×10^{20} cm^{-3}. The corresponding critical density from these measurements is estimated as $n_c = F_c(1-R)\eta\lambda/hcd \approx 2\times10^{21}$ cm^{-3}, in fair agreement. The transition to the *Immm* phase is expected to cause band structure renormalization and a closure of the electronic band gap, leading to semimetallic electronic dispersion [31]. A transition to a semimetallic band structure could explain the fixed finite-frequency

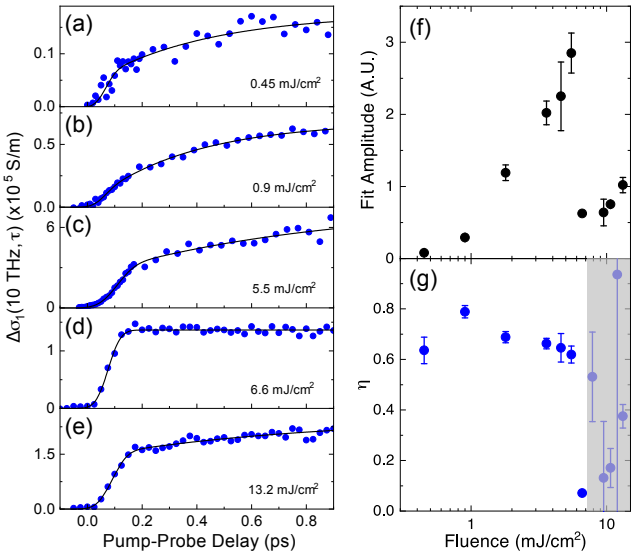

Figure 3. (a-e) $\Delta\sigma_1(\omega,\tau)$ dynamics at $\omega/2\pi = 10$ THz for indicated pump fluences F. Rate equation model fits (Eqn. 3) are shown as black lines. Note the differences in vertical axis scaling. (f) $\Delta\sigma_1$(10 THz, 1 ps) as a function of pump fluence, showing approximately linear scaling below F_c and a sharp drop with little scaling above F_c. (g) Fitted proportion of carriers deposited in band extrema η (Eqn. 3) as a function of fluence showing sharp drop near F_c.

spectral peak above F_c as a new interband THz absorption would appear in the mid-IR. Additional support for this idea is the relatively fluence-independent conductivity above F_c shown in Fig. 2(d), which would would be expected for a system whose gap is collapsed as excitation only serves to heat the charge distribution. While a recent time-resolved ARPES study of SnSe observed some evidence of spectral weight within the gap as early as 40 fs following photoexcitation, the 800 nm excitation fluence was significantly below F_c at 0.95 mJ/cm[57].

In conclusion, time-resolved THz spectroscopy was used to probe the ultrafast electronic response of SnSe under fs optical excitation. The transient THz optical conductivity was Lorentzian in character whose resonant frequency is carrier density dependent. This suggests photocarrier localization into heterogeneous conducting domains and phase co-existence on the nanoscale, driven by optical excitation and the removal of bonding electrons. Bimodal photoconductivity dynamics were observed and could be explained by multi-valley excitation into both free and localized states related to the non-dispersive bands derived from the Sn 5s-Se 4p hybridization. At a critical fluence of

$F_c \approx 6$ mJ/cm^2, the spectra, dynamics, and magnitude of the THz conductivity change drastically indicating a macroscopic change of phase. The vanishing of intervalley scattering and the near constant conductivity magnitude with further increase of pump fluence suggests a collapse of the band gap, which is consistent with a recent study suggesting SnSe moves towards a thermally inaccessible *Immm* phase. This motivates further high fluence TR-ARPES measurements and time-resolved spatial probes of nanoscale conductivity to potentially resolve this novel, transient phase of SnSe.

ACKNOWLEDGMENTS

BJD and DGC are grateful for the SnSe electronic band structure data from Ref. [5] provided by D. Rybkovskiy and for conversations with B. Siwick. This work was supported through funding by NSERC and Mitacs programs. The Northwestern University personnel and research work was supported by the Department of Energy, Office of Science, Basic Energy Sciences under Grant DE-SC0024256 (design and synthesis of thermoelectric materials).

* Correspondence email address: david.cooke2@mcgill.ca

[1] L. D. Zhao, S. H. Lo, Y. S. Zhang, H. Sun, G. J. Tan, C. Uher, C. Wolverton, V. P. Dravid, and M. G. Kanatzidis, Nature **508**, 373 (2014).
[2] R. Q. Guo, X. J. Wang, Y. D. Kuang, and B. L. Huang, Phys. Rev. B **92**, 115202 (2015).
[3] C. Chang, G. J. Tan, J. Q. He, M. G. Kanatzidis, and L. D. Zhao, Chem. Mater. **30**, 7355 (2018).
[4] M. M. Alsalama, H. Hamoudi, A. Abdala, Z. K. Ghouri, and K. M. Youssef, Rev. Adv. Mater. Sci. **59**, 371 (2020).
[5] V. Tayari, B. Senkovskiy, D. Rybkovskiy, N. Ehlen, A. Fedorov, C.-Y. Chen, J. Avila, M. Asensio, A. Perucchi, and P. Di Pietro, Phys. Rev. B **97**, 045424 (2018).
[6] K. Patel, G. Solanki, K. Patel, V. Pathak, and P. Chauhan, Eur. Phys. J. B **92**, 1 (2019).
[7] T. Q. Dang, Phys. Status Solidi A **86**, 421 (1984).
[8] J. M. Skelton, L. A. Burton, S. C. Parker, A. Walsh, C. E. Kim, A. Soon, J. Buckeridge, A. A. Sokol, C. R. A. Catlow, A. Togo, and I. Tanaka, Phys. Rev. Lett. **117**, 075502 (2016).
[9] D. Bansal, J. W. Hong, C. W. Li, A. F. May, W. Porter, M. Y. Hu, D. L. Abernathy, and O. Delaire, Phys. Rev. B **94**, 054307 (2016).
[10] G. D. Tang, J. Liu, J. Zhang, D. Li, K. H. Rara, R. Xu, W. Q. Lu, J. Z. Liu, Y. S. Zhang, and Z. Z. Peng, ACS Appl. Mater. Interfaces **10**, 30558 (2018).
[11] C. Chang and L. D. Zhao, Mater. Today Phys. **4**, 50 (2018).
[12] F. Liu, P. Parajuli, R. Rao, P. C. Wei, A. Karunarathne, S. Bhattacharya, R. Podila, J. He, B. Maruyama, G. Priyadarshan, J. R. Gladden, Y. Y. Chen, and A. M. Rao, Phys. Rev. B **98**, 224309 (2018).
[13] J. Hong and O. Delaire, Mater. Today Phys. **10**, 100093 (2019).
[14] P. Wu, F. R. Fan, M. Hagihala, M. Kofu, K. L. Peng, Y. Ishikawa, S. Lee, T. Honda, M. Yonemura, K. Ikeda, T. Otomo, G. Y. Wang, K. Nakajima, Z. Sun, and T. Kamiyama, New J. Phys. **22**, 083083 (2020).
[15] Y. Lu, F. W. Zheng, Y. Yang, P. Zhang, and D. B. Zhang, Phys. Rev. B **103**, 014304 (2021).
[16] B. Jiang, J. Neu, D. Olds, S. A. Kimber, K. Page, and T. Siegrist, Nat. Commun. **14**, 3211 (2023).
[17] T. Chattopadhyay, J. Pannetier, and H. G. Vonschnering, J. Phys. Chem. Solids **47**, 879 (1986).
[18] U. Aseginolaza, R. Bianco, L. Monacelli, L. Paulatto, M. Calandra, F. Mauri, A. Bergara, and I. Errea, Phys. Rev. Lett. **122**, 075901 (2019).
[19] T. Lanigan-Atkins, S. Yang, J. L. Niedziela, D. Bansal, A. F. May, A. A. Puretzky, J. Y. Y. Lin, D. M. Pajerowski, T. Hong, S. Chi, G. Ehlers, and O. Delaire, Nat. Commun. **11**, 1 (2020).
[20] L. D. Zhao, C. Chang, G. J. Tan, and M. G. Kanatzidis, Energy Environ. Sci. **9**, 3044 (2016).
[21] Y. Xiao, C. Chang, Y. L. Pei, D. Wu, K. L. Peng, X. Y. Zhou, S. K. Gong, J. Q. He, Y. S. Zhang, Z. Zeng, and L. D. Zhao, Phys. Rev. B **94**, 125203 (2016).
[22] J. S. Kang, H. Wu, M. Li, and Y. J. Hu, Nano Lett. **19**, 4941 (2019).
[23] C. W. Li, J. Hong, A. F. May, D. Bansal, S. Chi, T. Hong, G. Ehlers, and O. Delaire, Nat. Phys. **11**, 1063 (2015).
[24] J. L. Ma, Y. N. Chen, and W. Li, Phys. Rev. B **97**, 205207 (2018).
[25] Y. Lan, B. J. Dringoli, D. A. Valverde-Chávez, C. S. Ponseca, M. Sutton, Y. He, M. G. Kanatzidis, and D. G. Cooke, Sci. Adv. **5**, eaaw5558 (2019).
[26] M. R. Otto, L. P. René de Cotret, D. A. Valverde-Chavez, K. L. Tiwari, N. Émond, M. Chaker, D. G. Cooke, and B. J. Siwick, PNAS **116**, 450 (2019).
[27] M. Liu, H. Y. Hwang, H. Tao, A. C. Strikwerda, K. Fan, G. R. Keiser, A. J. Sternbach, K. G. West, S. Kittiwatanakul, and J. Lu, Nature **487**, 345 (2012).
[28] D. Fausti, R. Tobey, N. Dean, S. Kaiser, A. Dienst, M. C. Hoffmann, S. Pyon, T. Takayama, H. Takagi, and A. Cavalleri, Science **331**, 189 (2011).
[29] W. Wang, L. Wu, J. Li, N. Aryal, X. Jin, Y. Liu, M. Fedurin, M. Babzien, R. Kupfer, and M. Palmer, npj Quantum Mater. **6**, 1 (2021).
[30] L. P. René de Cotret, M. R. Otto, J.-H. Pöhls, Z. Luo, M. G. Kanatzidis, and B. J. Siwick, PNAS **119**, e2113967119 (2022).
[31] Y. Huang, S. Yang, S. Teitelbaum, G. De la Peña, T. Sato, M. Chollet, D. Zhu, J. L. Niedziela, D. Bansal, A. F. May, A. M. Lindenberg, O. Delaire, D. A. Reis, and M. Trigo,

Phys. Rev. X **12**, 011029 (2022).
[32] Y. Huang, S. Teitelbaum, S. Yang, G. De la Peña, T. Sato, M. Chollet, D. Zhu, J. L. Niedziela, D. Bansal, A. F. May, A. M. Lindenberg, O. Delaire, M. Trigo, and D. A. Reis, Phys. Rev. Lett. **131**, 156902 (2023).
[33] Y. Han, J. Yu, H. Zhang, F. Xu, K. Peng, X. Zhou, L. Qiao, O. V. Misochko, K. G. Nakamura, and G. M. Vanacore, J. Phys. Chem. Lett. **13**, 442 (2022).
[34] J. Dai, X. Xie, and X.-C. Zhang, Phys. Rev. Lett. **97**, 103903 (2006).
[35] D. Cook and R. Hochstrasser, Opt. Lett. **25**, 1210 (2000).
[36] K.-Y. Kim, J. H. Glownia, A. J. Taylor, and G. Rodriguez, IEEE J. Quantum Electron. **48**, 797 (2012).
[37] M. D. Thomson, V. Blank, and H. G. Roskos, Opt. Express **18**, 23173 (2010).
[38] P. U. Jepsen, D. G. Cooke, and M. Koch, Laser Photonics Rev. **5**, 124 (2011).
[39] I.-C. Ho, X. Guo, and X.-C. Zhang, Opt. Express **18**, 2872 (2010).
[40] K. Iwaszczuk, D. G. Cooke, M. Fujiwara, H. Hashimoto, and P. U. Jepsen, Opt. Express **17**, 21969 (2009).
[41] H. Němec, F. Kadlec, and P. Kužel, J. Chem. Phys. **117**, 8454 (2002).
[42] J. Orenstein and J. Dodge, Phys. Rev. B **92**, 134507 (2015).
[43] A. S. Chaves, R. L. Gonzalez-Romero, J. J. Melendez, and A. Antonelli, Phys. Chem. Chem. Phys. **23**, 900 (2021).
[44] I. Efthimiopoulos, M. Berg, A. Bande, L. Puskar, E. Ritter, W. Xu, A. Marcelli, M. Ortolani, M. Harms, J. Muller, S. Speziale, M. Koch-Muller, Y. Liu, L. D. Zhao, and U. Schade, Phys. Chem. Chem. Phys. **21**, 8663 (2019).
[45] F. A. Hegmann and K. P. Lui, in *Ultrafast Phenomena in Semiconductors VI*, Vol. 4643 (SPIE, 2002) pp. 31–41.
[46] L. Makinistian and E. A. Albanesi, Phys. Status Solidi B **246**, 183 (2009).
[47] G. M. Wang, W. F. Zhang, F. Xing, K. Z. Han, H. N. Zhang, and S. G. Fu, Infrared Phys. Technol. **108**, 103349 (2020).
[48] P. Kužel and H. Němec, J. Phys. D: Appl. Phys. **47**, 374005 (2014).
[49] W. H. Sio and F. Giustino, Nat. Phys. , 1 (2023).
[50] F. Caruso, M. Troppenz, S. Rigamonti, and C. Draxl, Phys. Rev. B **99**, 081104 (2019).
[51] K. Lee, A. J. Heeger, and Y. Cao, Phys. Rev. B **48**, 14884 (1993).
[52] N. V. Smith, Phys. Rev. B **64**, 155106 (2001).
[53] H. J. Joyce, J. L. Boland, C. L. Davies, S. A. Baig, and M. B. Johnston, Semicond. Sci. Tech. **31**, 103003 (2016).
[54] T. W. Yan, Y. P. Han, Q. Fu, T. T. Xu, S. W. Yin, W. Z. Wu, and W. L. Liu, Opt. Mater. **108**, 110440 (2020).
[55] A. Das, A. Kumar, and P. Banerji, J. Phys. Condens. Matter **32**, 265502 (2020).
[56] J. Shah, B. Deveaud, T. C. Damen, W. T. Tsang, A. C. Gossard, and P. Lugli, Phys. Rev. Lett. **59**, 2222 (1987).
[57] M. Okawa, Y. Akabane, M. Maeda, G. Tan, L.-D. Zhao, M. G. Kanatzidis, T. Suzuki, M. Watanabe, J. Xu, and Q. Ren, Scr. Mater. **223**, 115081 (2023).